Supporting Information

Converting biomass eggplant into multifunctional porous carbon electrodes for self-powered capacitive deionization

Cuijiao Zhao,[†,‡,1] Shengbo Zhang,[†,‡,1] Na Sun,[†,‡] Hongjian Zhou,[†,*] Guozhong Wang,[†]

Yunxia Zhang,[†] Haimin Zhang[†,*] and Huijun Zhao[†,§]

[†] Key Laboratory of Materials Physics, Centre for Environmental and Energy Nanomaterials, Anhui Key Laboratory of Nanomaterials and Nanotechnology, CAS Center for Excellence in Nanoscience, Institute of Solid State Physics, Chinese Academy of Sciences, Hefei 230031, China

[‡] University of Science and Technology of China, Hefei 230026, China

[§] Centre for Clean Environment and Energy, Griffith University, Gold Coast Campus, QLD 4222, Australia

[1] These authors contributed equally to this work.

Corresponding Author

* E-mail: hjzhou@issp.ac.cn (H. Zhou); zhanghm@issp.ac.cn (H. Zhang)

EXPERIMENTAL SECTION

Chemicals and materials. Sodium chloride (NaCl), potassium bicarbonate ($KHCO_3$), chloride acid (HCl) and nitric acid (HNO_3) were supplied by Sinopharm Chemical Reagent Co., Ltd. Cadmium chloride ($CdCl_2$) and lead nitrate ($Pb(NO_3)_2$) were bought from Aladdin Chemical Reagent Co., Ltd. Carbon paper (HCP030N) was used as received from Shanghai Hesen electric Co., Ltd. Eggplant was purchased from local market (Hefei, China) and deionized water (18 MΩ) was used in all experiments.

Characterization. Scanning electron microscopy (SEM) measurements of the samples were performed with a field emission scanning electron microscope (FESEM, Quanta 200FEG) at an acceleration voltage of 5.0 kV. Transmission electron microscopy (TEM) images of the samples were recorded on a JEOL-2010 microscope operated at an accelerating voltage of 200 kV. The crystalline structures of the samples were identified by X-ray diffraction (XRD, Philips X'pert PRO) using Ni-filtered monochromatic Cu Kα radiation (λ Kα1=1.5418 Å) at 40 kV and 40 mA. Raman spectra of the samples were recorded on a Renishaw Micro-Raman Spectroscopy (Renishaw inVia Reflex) using 532 nm laser excitation. Fourier transform infrared (FT-IR) spectra of the samples were recorded on a Perkin-Elmer TGA 7 infrared spectrometer to identify the surface functional groups of the samples. Nitrogen adsorption-desorption isotherms of the samples were measured using an automated gas sorption analyzer (Autosorb-iQ-Cx). X-ray photoelectron spectroscopy (XPS) analysis of the samples was performed on an ESCALAB 250 X-ray

photoelectron spectrometer (Thermo, America) equipped with Al Kα1, 2 monochromatized radiations at 1486.6 eV X-ray source. The thermalgravimetric analysis (TGA) was performed on a TGA Pyris 1 under nitrogen atmosphere at a heating rate of 10 $^{\circ}C \cdot min^{-1}$. The Pb^{2+} and Cd^{2+} concentrations in water after the capacitive removal were determined by inductively coupled plasma mass spectrum (ICP-MS iCAP RQ, Thermo Fisher Scientific). The contact angles were measured using a Kruss DSA 30 Contact angle tester.

Electrochemical measurements. The capacitance and galvanostatic charge/discharge measurements of the samples were performed in 1.0 $mol \cdot L^{-1}$ NaCl solution on a CHI 660E electrochemical workstation (CHI 660E, CH Instrument, Inc., shanghai, China), using a three-electrode configuration consisted of a working electrode, an Ag/AgCl reference electrode and a Pt counter electrode. The cyclic voltammetry (CV) and galvanostatic charge/discharge (GCD) measurements were carried out in the potential range of 0 ~ 1.0 V and -1.0 ~ -0.2 V, respectively. Electrochemical impedance spectroscopy (EIS) measurement was conducted with an amplitude of 5.0 mV and the frequency range from 100 KHz to 0.01 Hz. The specific capacitance (C) was calculated from GCD curves according to the following equation:

$$C = I\Delta t / m\Delta V \qquad (1)$$

where I is the discharge current density, Δt is the discharge time, m is the mass of the active material, and ΔV is the discharge voltage difference.

The measurements of oxygen reduction reaction (ORR) performance of the samples were carried out on an electrochemical station (CHI 660E, CH Instrument,

Inc., shanghai, China) combined with a PINE rotating disk electrode (RDE) system (Pine Instruments Co. Ltd. USA). A glassy carbon (GC) electrode (5.0 mm in diameter) served as the substrate of electrocatalyst was used as the working electrode. Ag/AgCl and Pt wire were used as the reference electrode and the counter electrode, respectively. A conventional three-electrode electrochemical cell with a flowing gas system was applied for electrochemical measurements. Prior to use, the GC electrode was sequentially polished with a 5.0, 3.0, and 0.05 μm alumina slurry and then washed ultrasonically in water and ethanol. The cleaned electrode was dried with a high-purity nitrogen stream. The eggplant-derived NPC catalyst ink was prepared by dispersing the NPC catalyst powder (10 mg) into a mixture containing 100 μL of Nafion solution (0.5 wt.%) and 900 μL of ethanol, followed by a ultrasonic treatment for 2 min. Then, 12 μL of the catalyst ink was cast onto the GC electrode surface and dried at room temperature for further measurement.

The ORR performance of eggplant-derived NPC catalyst was measured by linear sweep voltammetry (LSV) in an O_2-saturated 0.1 M KOH solution. The LSV curves were measured from 0.2 to -0.8 V at a scan rate of 10 mV s^{-1} with different disk rotation rates of 400, 625, 900, 1225, 1600 and 2025 rpm. The electron transfer number (*n*) *per* oxygen molecule in an ORR process was calculated by the Koutecky-Levich (*K-L*) equations [1-2]:

$$J^{-1} = J_k^{-1} + (B\omega^{1/2})^{-1} \quad (2)$$

$$B = 0.62nF(D_0)^{2/3}\nu^{-1/6}C_0 \quad (3)$$

$$J_\kappa = nFkC_0 \quad (4)$$

where J is the measured current density during ORR, J_k is the kinetic current density, ω is the electrode rotating angular velocity (ω=2πN, where N is the linear rotation speed), B is the slope of the *K-L* plots, F is the Faraday constant (F=96, 485 $C \cdot mol^{-1}$), D_0 is the diffusion coefficient of O_2 in 0.1 M KOH (1.9×10^{-5} $cm^2 \cdot s^{-1}$), v is the kinetic viscosity (0.01 $cm^2 \cdot s^{-1}$), and C_0 is the bulk concentration of O_2 (1.2×10^{-3} $mol \cdot L^{-1}$).

The oxygen evolution reaction (OER) polarization curve of eggplant-derived NPC catalyst was measured on an electrochemical station (CHI 660E, CH Instrument, Inc., shanghai, China) with a scan rate of 5.0 $mV \cdot s^{-1}$ at room temperature in 1.0 M KOH. The potential was with *iR*-compensated. And the presented current density was normalized to the geometric surface area.

The measurements of the Zn-air batteries were performed using home-built electro-chemical cells [3]. All data were collected from the as-fabricated cell with a CHI 660E electrochemical workstation (CH Instruments, Inc., Shanghai, China) at room temperature. Briefly, zinc foil was used as the anode and the eggplant-derived NPC catalyst loaded onto the gas diffusion layer (Teflon-coated carbon fiber paper with a geometric area of 1.0 cm^2, the catalyst loading amount was ~2.0 $mg \cdot cm^{-2}$) was used as the air cathode. The electrolyte was 6.0 M KOH and 0.2 M zinc acetate solution.

Measurement of CDI performances: The CDI testing apparatus consisted of a pump, a conductivity meter, an electrical power supply, a home-made CDI unit, a feed water reservoir and CHI 660E electrochemical workstation (CH Instruments, Inc., Shanghai, China). During CDI measurements, carbon paper (HCP030N, density:

0.78g/cm^3; thickness: 0.30±0.01 mm) was used as current collector, and silicon spacer with a thickness of 1.0 mm was used for separating the cathode and anode. During the CDI measurements, a conductivity meter (Type DDSJ-308A, Leici Company) was located in NaCl stock solution to monitor the variation of the solution conductivity with operation time. The conductivity of NaCl solution was recorded every 20 s in the adsorption and desorption processes. The salt adsorption capacity (SAC) was calculated according to the following equation:

$$\Gamma = {(C_0 - C)V}/{m} \quad (1)$$

where Γ is the salt adsorption capacity; C_0 and C are the initial and final salt concentrations, respectively; V is the total volume of NaCl solution; and m represents the total mass of the active components including anode and cathode.

The average salt adsorption rate (ν) of CDI electrode materials was calculated according to the following equation:

$$\nu = {\Gamma}/{t} \quad (2)$$

where ν is the average salt adsorption rate, Γ is the salt adsorption capacity and t is the total cycling time including adsorption and desorption.

The charge e□ciency (Λ) is a functional tool to gain insight into the electric double layer formed at the interface between the electrode and electrolyte solution, as described according to the following equation:

$$\Lambda = \frac{\Gamma \times F}{\Sigma} \quad (3)$$

where F is the Faraday constant (96485 C·mo^{l-1}), Γ is the adsorption capacity (mol·g^{-1})

and Σ (charge, $C \cdot g^{-1}$) was obtained by integrating the corresponding current.

Table S1. Elemental composition analysis of NC-800 and NPC-800 by XPS technique.

Sample	C (at.%)	O (at.%)	N (at.%)	Pyridinic-N (at.%)	Pyrrolic - N (at.%)	Graphitic-N (at.%)
NC-800	86.00	9.29	4.71	26.28	40.02	33.69
NPC-800	75.99	21.34	2.67	33.22	14.87	46.67

Table S2. Performance comparison of NPC-800 assembled CDI and most recently reported carbon-based CDI.

Sample	Applied voltage (V)	Initial salt concentration ($mg \cdot L^{-1}$)	Desalination capacity ($mg \cdot g^{-1}$)	Ref.
OMC/CNT	1.2	40	0.69	4
GO	2.0	250	8.60	5
3D graphene	1.4	500	13.72	6
Graphene/CNTS/AC	1.2	50	2.30	7
HCPs	1.4	40	34.27	8
$Na_4Mn_9O_{18}$ //AC	1.2	35.73	31.20	9
PCS	1.2	500	15.80	10
MMC	1.4	1000	20.78	11
CCS	1.2	500	16.10	12
WCF	1.2	100	5.7	13
PGF	1.4	500	19.1	14
PC800	1.4	500	25.16	15
NP-3DHCA	1.2	500	26.8	16
GSSNA-11	1.2	500	22.09	17
MOx/CNTf	1.2	2000	6.5	18
This work	1.2	500	31.9	-

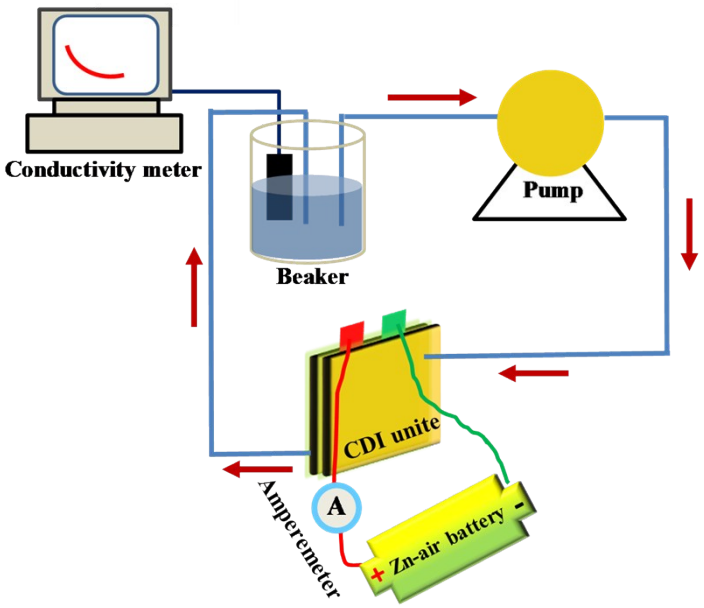

Scheme S1. A schematic illustration of Zn-air battery driven CDI device setup.

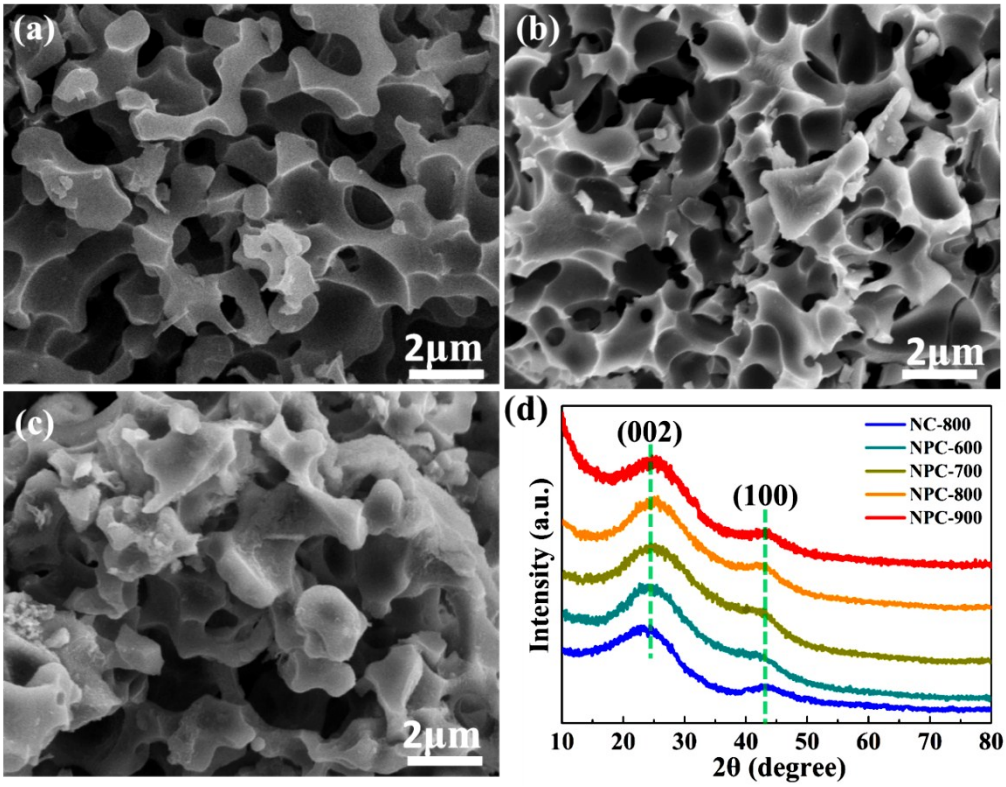

Figure S1. SEM images of eggplant-derived N, O-containing porous carbon with the assistance of $KHCO_3$ during pyrolysis. (a) NPC-600, (b) NPC-700 and (c) NPC-900. (d) XRD patterns of NC-800, NPC-600, NPC-700, NPC-800 and NPC-900.

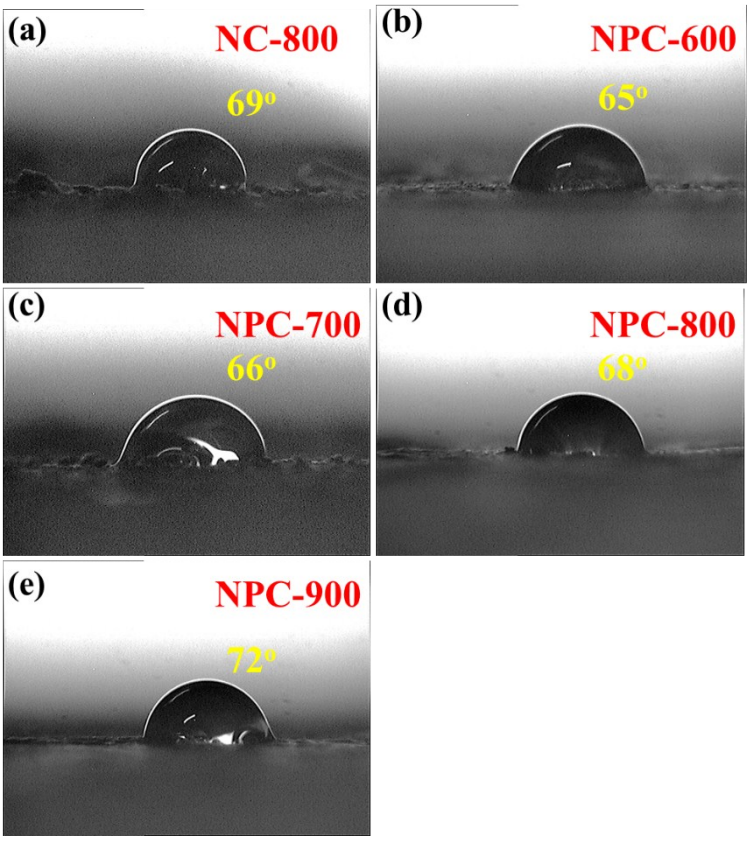

Figure S2. Static contact angle measurements of (a) NC-800, (b) NPC-600, (c) NPC-700, (d) NPC-800 and (e) NPC-900.

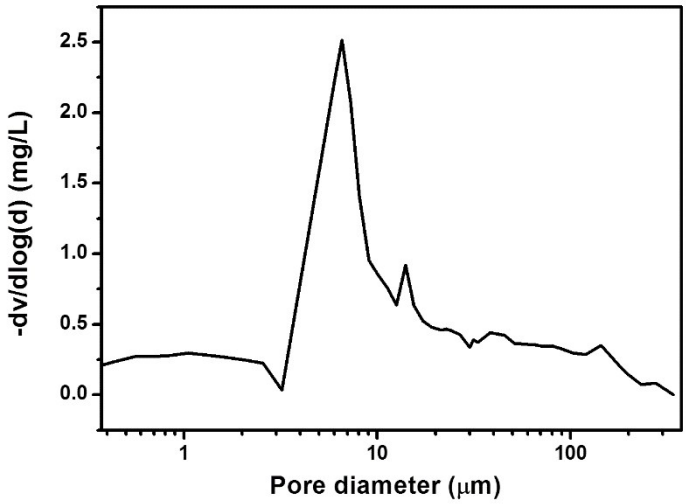

Figure S3. Macropore size distribution curve by mercury porosimetry.

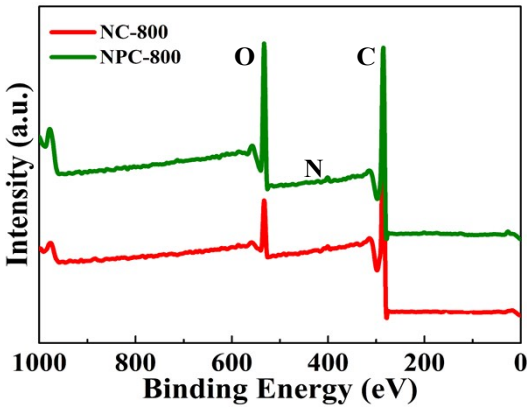

Figure S4. Surface survey XPS spectra of NC-800 and NPC-800.

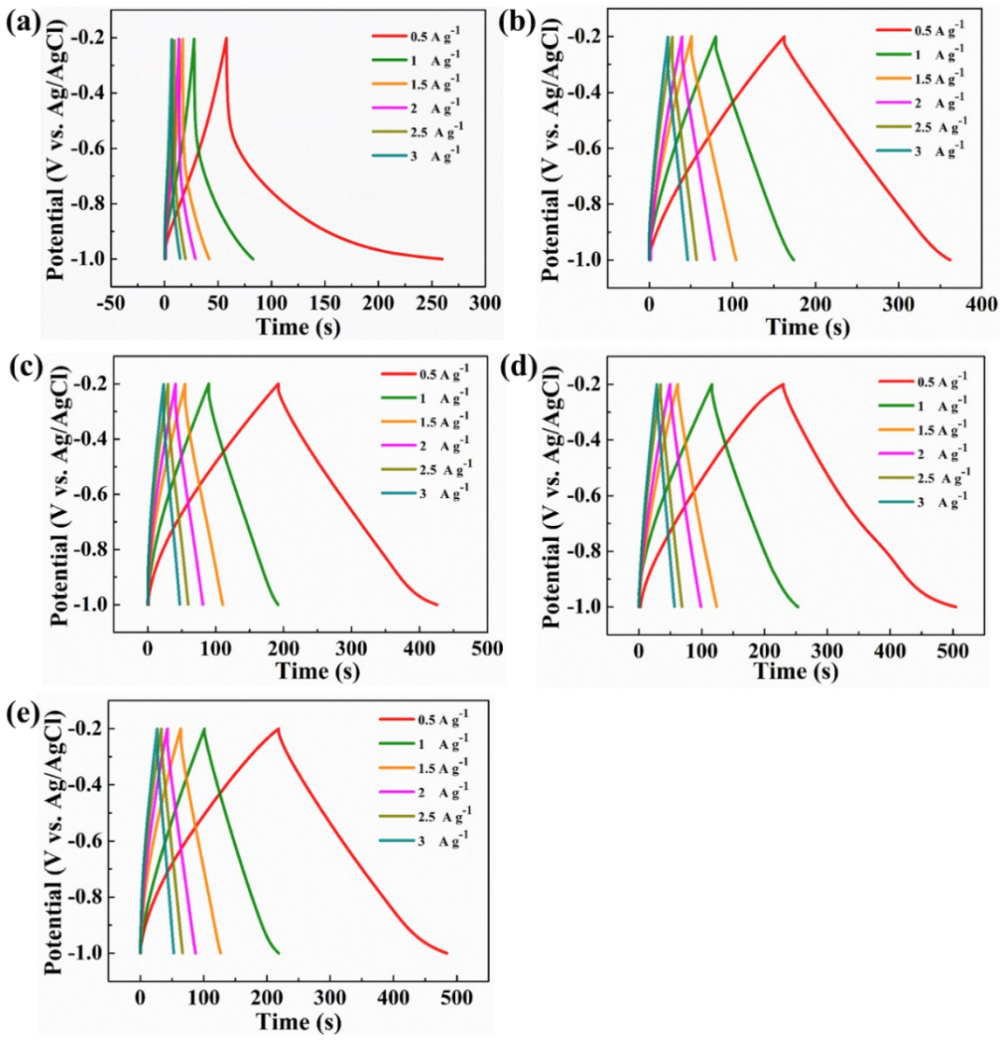

Figure S5. GCD curves of eggplant-derived N, O-containing porous carbon electrodes. (a) NC-800, (b) NPC-600, (c) NPC-700, (d) NPC-800 and (e) NPC-900 in 1.0 mol·L^{-1} NaCl solution over a potential range from -1.0 to -0.2 V at different current densities.

The capacitance and galvanostatic charge/discharge measurements of the samples were performed in 1.0 mol·L^{-1} NaCl solution on a CHI 660E electrochemical workstation (CHI 660E, CH Instrument, Inc., shanghai, China), using a three-electrode configuration consisted of the two electrodes of CDI unite and an Ag/AgCl reference electrode. The cyclic voltammetry (CV) and galvanostatic charge/discharge (GCD) measurements were carried out in the potential range of 0~1.5 V and 0~1 V, respectively.

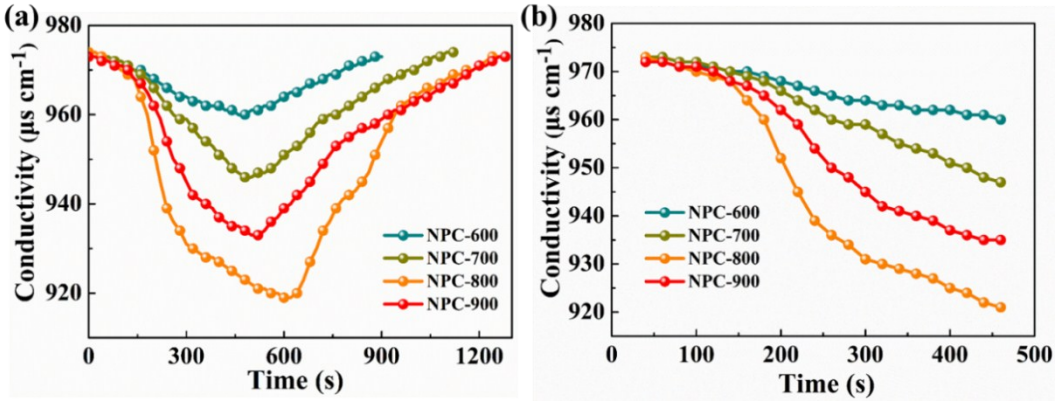

Figure S6. (a) Adsorption and desorption curves and (b) plots of NaCl solution conductivity *vs*. operation time of NPC-600, NPC-700, NPC-800 and NPC-900 electrodes at 1.2 V in NaCl solution with an initial concentration of 500 mg·L^{-1}.

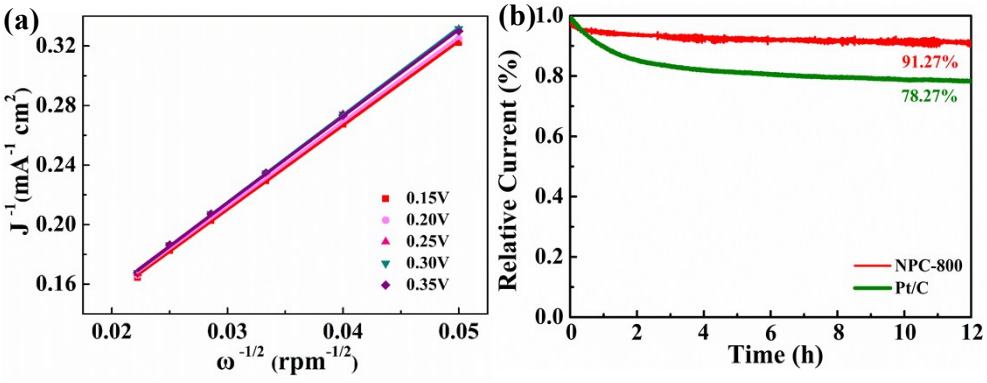

Figure S7. (a) K-L plots of NPC-800 derived from Figure 6a at different potentials. (b) Durability tests of NPC-800 and commercial Pt/C catalysts at an applied potential of -0.35 V with a rotation speed of 1600 rpm.

References:

[1] Gong K.P, Du F, Xia Z.H, et al. Nitrogen-doped carbon nanotube arrays with high electrocatalytic activity for oxygen reduction. Science 2009; 323:760-764.

[2] Qu L.T, Liu Y, Baek J.B, et al. Nitrogen-doped graphene as efficient metal-free electrocatalyst for oxygen reduction in fuel cells. ACS Nano 2010; 3:1321-1326.

[3] Wu Z. Y, Xu X. X, Hu B. C, et al. Iron carbide nanoparticles encapsulated in mesoporous Fe-N-doped carbon nanofibers for efficient electrocatalysis. Angew Chem Int Ed Engl 2015; 54:8179-83.

[4] Peng Z, Zhang D, Yan T, et al. Three-dimensional micro/mesoporous carbon composites with carbon nanotube networks for capacitive deionization. Appl Surf Sci 2013; 282: 965-973.

[5] Jia B, Zou L. Graphene nanosheets reduced by a multi-step process as high-performance electrode material for capacitive deionisation. Carbon 2012; 50:2315-2321.

[6] Liu P, Wang H, Yan T, et al. Grafting sulfonic and amine functional groups on 3D graphene for improved capacitive deionization. J Mater Chem A 2016; 4:5303-5313.

[7] Zhu G, Wang W, Li X, et al. Design and fabrication of a graphene/carbon nanotubes/activated carbon hybrid and its application for capacitive deionization. RSC Adv 2016; 6:5817-5823.

[8] Chao L, Liu Z, Zhang G, et al. Enhancement of capacitive deionization capacity of hierarchical porous carbon. J Mater Chem A 2015; 3:12730-12737.

[9] Lee J, Kim S, Kim C, et al. Hybrid capacitive deionization to enhance the desalination performance of capacitive techniques. Energy Environ Sci 2014; 7:3683-3689.

[10] Leong Z. Y, Yang H. Y. Porous carbon hollow spheres synthesized via a modified Stöber method for capacitive deionization. RSC Adv 2016; 6:53542-53549.

[11] Xu D, Tong Y, Yan T, et al. N,P-codoped meso-/microporous carbon derived from biomass materials via a Ddual-activation strategy as high-performance electrodes for deionization capacitors. ACS Sustain Chem Eng 2017; 5:5810-5819.
[12] Li G.-X, Hou P.-X, Zhao S.-Y, et al. A flexible cotton-derived carbon sponge for high-performance capacitive deionization. Carbon 2016; 101:1-8.
[13] Liu M, Xu M, Xue Y, et al. Efficient capacitive deionization using natural basswood-derived, freestanding, hierarchically porous carbon electrodes. ACS Appl Mater Interfaces 2018; 10:31260-31270.
[14] Duan H, Yan T, Chen G, et al. A facile strategy for the fast construction of porous graphene frameworks and their enhanced electrosorption performance. Chem Commun 2017; 53:7465-7468.
[15] Wang Z, Yan T, Chen G, et al. High salt removal capacity of metal–organic gel derived porous carbon for capacitive deionization. ACS Sustain Chem Eng 2017; 5:11637-11644.
[16] Han J, Shi L, Yan T, et al. Removal of ions from saline water using N, P co-doped 3D hierarchical carbon architectures via capacitive deionization. Energy Environ Sci 2018; 5:2337-2345.
[17] Khan Z. U, Yan T, Shi L, et al. Improved capacitive deionization by using 3D intercalated graphene sheet–sphere nanocomposite architectures. Energy Environ Sci 2018; 5:980-991.
[18] Santos C, Lado J. J, García-Quismondo E, et al. Interconnected metal oxide CNT fibre hybrid networks for current collector-free asymmetric capacitive deionization. J Mater Chem A 2018; 6*:*10898-10908.